Combined effect of pump-light intensity and modulation field on the performance of optically pumped magnetometers under zero-field parametric modulation

Jing Wang, Wenfeng Fan, Kaifeng Yin, and Yeguang Yan
School of Instrumentation Science and Optoelectronics Engineering, Beihang University, Beijing 100191, China and Hangzhou Innovation Institute of Beihang University, Hangzhou 310051, China

Binquan Zhou* and Xinda Song†
Research Institute of Frontier Science, Beihang University, Beijing 100191, China and Beijing Advanced Innovation Center for Big Data-Based Precision Medicine, Beihang University, Beijing, 100191, China

(Received 30 December 2019; accepted 17 April 2020; published 19 May 2020)

This paper investigates the performance optimization of optically pumped magnetometers under zero-field parametric modulation. Based on the analytical solutions of the Bloch equation, both longitudinal and transverse modulations are studied experimentally. To estimate the nonuniform polarization distribution of alkali-metal atoms in the vapor cell, an average pumping rate model is proposed. Furthermore, the accuracy of this model and the measurement of the transverse relaxation rate are verified via the agreement between experimental and theoretical values. The results indicate that optimal performance can be achieved by employing a suitable modulation field, the selection of which is related to the modulation index u in the Bessel series and the pump-light intensity. Although both operating modes show similar responses to weak magnetic fields, their effects on pump-light intensity are different due to the means of detecting atomic polarization. An optimal value of the pump-light intensity on the response strength exists in longitudinal modulation. However, with regard to transverse modulation, the sensitivity under weak pump-light intensity is better. This research has far-reaching significance for cases when the parametric modulation is manipulated.

DOI: 10.1103/PhysRevA.101.053427

I. INTRODUCTION

Optically pumped magnetometers (OPMs) hold the promise of excellent sensitivity for the detection of weak magnetic fields [1]. Since their development [2–4], they have been investigated intensively, and a variety of types have been reported [5–7]. Traditional OPMs are typically operated in the geomagnetic field, such as Mx and Mz magnetometers that utilize the technique of magnetic resonance to observe the Larmor frequency [8–10]. Their fundamental sensitivity is limited by the spin-exchange relaxation [11]; therefore, it is difficult to meet the demands of biomagnetism measurement. To obtain subfemtotesla sensitivity, Kominis *et al.* proposed a spin-exchange-relaxation-free (SERF) magnetometer [12], which surpassed the superconducting quantum interference devices (SQUIDs).

Another core branch is zero-field parametric modulation, which emerged in the 1970s [13,14] and was recently operated in the SERF regime [15]. Parametric modulation forces optically pumped atoms to precess at a frequency consistent with the modulation field of several kilohertz. Because of the inherent technical suppression of low-frequency noises, this has become a research hot spot [16,17]. Especially in magnetoencephalography, OPMs offer the advantages of noncryogenic operation and wearable system construction compared with SQUIDs [18] and have been developed rapidly [19,20].

Two structures of zero-field parametric modulation have been developed depending on the modulation direction. The parametric modulation scheme with a longitudinal modulation field along the direction of the pump light (z axis) is named the Z mode. The transverse modulation field in the plane perpendicular to the pump beam is named the X mode. The X mode is superior in compact miniaturization where one laser beam is sufficient to detect weak magnetic fields [21]. Several micromachined OPMs have been proposed with the X mode [22–25]. The Z mode was first introduced in the SERF regime in 2006 by the Walker group, who demonstrated that parametric modulation resulted in only a slight loss of sensitivity compared with a nonmodulated SERF magnetometer [26]. This can enable simultaneous detection of the two magnetic components B_x and B_y with one probe beam. Later, Zhang *et al.* developed a multichannel magnetometer and realized simultaneous multilocation magnetic-field measurements [27]. In either case, due to the presence of the modulation field, final analytical solutions of atomic responses can be expanded into the superposition of multiple harmonics with Bessel series by employing the Jacobi-Anger expansion. However, few studies have provided comparative analyses of these two modes, and the optimization of their sensitivity requires theoretical support.

The pursuit of sensitivity in OPMs follows a process of optimizing the polarization of an alkali metal to maximize

*bqzhou@buaa.edu.cn
†songxinda@buaa.edu.cn

its response while suppressing the system noise as much as possible. Hence, the ultimate goal is to improve the signal-to-noise ratio. Theoretical research indicates that the polarization is mainly determined by both the spin relaxation rate and the pumping rate [28]. The influences of cell temperature [29], pump beam diameter [30], and pump-power density [31] on the polarization were previously explored. In parametric modulation, the modulation field strength should be optimized to obtain the maximum value of the response coefficient according to the Bessel series [26]. However, this field will introduce extra spin-exchange relaxation [32], which affects the polarization. These issues have not been addressed so far in OPMs under zero-field parametric modulation.

In this paper, the combined effect of both the pump-light intensity and the modulation field on the signal-to-noise ratio performance of OPMs under zero-field parametric modulation is fully considered. This paper is organized as follows. First, the proposed average-pumping-rate model, a transverse relaxation-rate measurement method, and analytical solutions with theoretical models of the Z mode and the X mode are presented in Sec. II. According to these two operation modes, experimental setups constructed by a dual-beam structure and a single-beam structure are described in Sec. III. Relevant experiments were conducted under different pump-light intensities and different modulation fields. Results and a relevant discussion are presented in Sec. IV. The proposed theory has been verified and provides theoretical support for the improvement of OPM sensitivity.

II. THEORY ANALYSIS

The dynamics of optically pumped alkali vapor in the SERF regime can be described by a Bloch equation [28]:

$$\frac{\partial \mathbf{P}}{\partial t} = \frac{1}{q}[\gamma^e \mathbf{B} \times \mathbf{P} + R_{\mathrm{op}}(s\hat{z} - \mathbf{P}) - R_{\mathrm{tot}}\mathbf{P}], \tag{1}$$

where $\mathbf{P} = (P_x, P_y, P_z)$ is the electron polarization, q is the slowing-down factor, γ^e is the electron gyromagnetic ratio, $\mathbf{B}$ is the magnetic-field vector, R_{op} is the pumping rate, R_{tot} is the total spin-relaxation rate, and s is the photon spin vector of the pump beam.

For a potassium vapor, q can be represented as [33]

$$q = \frac{6 + 2P^2}{1 + P^2}. \tag{2}$$

R_{tot} consists of the following parts [34]:

$$R_{\mathrm{tot}} = \kappa_{SD}^{K} n_K + \kappa_{SD}^{He} n_{He} + \kappa_{SD}^{N2} n_{N2} + \frac{1}{T_2^{SE}} + \frac{1}{T_D}, \tag{3}$$

where κ is the binary spin-destruction coefficient, n is the number density for different components, $1/T_2^{SE}$ is the spin-exchange relaxation rate, and $1/T_D$ is the relaxation rate due to diffusion, which can be calculated as [30]

$$\frac{1}{T_D} = qD_{He}^{K}\left(\frac{\pi}{a}\right)^2, \tag{4}$$

where D_{He}^{K} is the diffusion constant of alkali atoms within the buffer gas and a is the equivalent radius of the vapor cell.

When a modulation field $B_m \cos(\omega_m t)$ is applied, the spin-exchange relaxation rate of K atomic spins is [32]

$$\frac{1}{T_2^{SE}(B_m)} = \frac{(\gamma^e B_m)^2}{R_{SE}}\left(\frac{1}{4} - \frac{4}{q^2}\right), \tag{5}$$

where $R_{SE} = \kappa_{SE}^{K} n_K$ is the spin-exchange rate and κ_{SE}^{K} is the spin-exchange coefficient.

The values of the parameters required in the above equations are given in Table I.

A. Average-pumping-rate model and its relationship with the spin-relaxation rate

Note that the pump intensity is attenuated by the absorption of the alkali vapor. Therefore, a position-dependent distribution of the pumping rate is achieved by using the Lambert-W function as [29]

$$R_{\mathrm{op}}(z) = R_{\mathrm{rel}} W\left[\frac{R_{\mathrm{op}}(0)}{R_{\mathrm{rel}}} \exp\left(\frac{R_{\mathrm{op}}(0)}{R_{\mathrm{rel}}} - n_K \sigma_{\mathrm{op}}(\nu) z\right)\right], \tag{6}$$

where R_{rel} is the sum of spin-relaxation rates that causes atomic spin depolarization and $\sigma_{\mathrm{op}}(\nu)$ is the optical pumping cross section related to the laser frequency ν. $R_{\mathrm{op}}(0)$ is the pumping rate at the entrance window of the vapor cell, which can be expressed as [30]

$$R_{\mathrm{op}}(0) = \frac{\sigma_{\mathrm{op}}(\nu)\phi(0)}{h\nu}, \tag{7}$$

where $\phi(0)$ is the initial pump-light power density and h is the Planck constant.

Since there is no depolarization in the spin-exchange collisions between alkali-metal atoms, the relationship between R_{tot} and R_{rel} can be expressed as

$$R_{\mathrm{tot}} = R_{\mathrm{rel}} + \frac{1}{T_2^{SE}(B_m)}. \tag{8}$$

As a nonuniform distribution, a uniform model [38] is no longer sufficiently to describe the phenomenon. To solve this problem, an average-pumping-rate model is proposed. The main idea of the developed average model is to estimate the pumping rate by summing $R_{\mathrm{op}}(z)$ along the z axis and dividing the result by the cell length L, which can be described by the following equation:

$$\overline{R_{\mathrm{op}}} = \frac{1}{L}\int_0^L R_{\mathrm{op}}(z)dz. \tag{9}$$

B. Z mode: Modulation field along the pump direction

Applying the z-axis modulation field $B_m \cos(\omega_m t)$ parallel to the pump light and operating in the zero field, components of $\mathbf{B}$ are $B_x = B_{x0}$, $B_y = B_{y0}$, and $B_z = B_m \cos(\omega_m t)$. The polarization projection is measured by a probe beam along the x axis, as shown in Fig. 1(a). Based on Eq. (1), the response of P_x for zero-order parametric modulation is observed to be

$$P_x(t) = \frac{P_0 \gamma^e J_0(u)}{\overline{R_{\mathrm{op}}} + R_{\mathrm{tot}}}\left\{2\sum_{k=1}^{k=\infty} J_{2k-1}(u)\sin[(2k-1)\omega_m t]B_{x0} + \left[J_0(u) + 2\sum_{k=1}^{k=\infty} J_{2k}(u)\cos(2k\omega_m t)\right]B_{y0}\right\}, \tag{10}$$

TABLE I. Parameters required for calculation.

Parameters	Value or expression	Reference
Spin-destruction rate coefficient of K-K: κ_{SD}^{K}	$1.0\times10^{-18}\bar{v}$ cm^3/s	[35]
Spin-destruction rate coefficient of K-N_2: κ_{SD}^{N2}	$7.9\times10^{-23}\bar{v}$ cm^3/s	[35]
Spin-destruction rate coefficient of K-He: κ_{SD}^{He}	$8.0\times10^{-25}\bar{v}$ cm^3/s	[36]
Spin-exchange rate coefficient of K-K: κ_{SE}^{K}	$1.8\times10^{-14}\bar{v}$ cm^3/s	[37]
Diffusion coefficient of K in He: D_{He}^{K}	$0.35\times(\frac{T}{273\text{ K}})^{\frac{3}{2}}\frac{1\text{ atm}}{P_{He}}$ cm^2/s	[36]

where $u=\frac{\gamma^e B_m}{q\omega_m}$ is the modulation index and $P_0=\frac{\overline{R_{\rm op}}}{\overline{R_{\rm op}}+R_{\rm rel}}$ is the approximate projection of P_z.

This indicates that the Z mode can realize the synchronous measurement of both B_x and B_y by the odd harmonics sensitive to B_{x0} and the even harmonics sensitive to B_{y0}. Since the increase of the harmonic order leads to a decrease in the response coefficient, only the dc component and first and second harmonics of ω_m are generally considered, with expressions of

$$P_{x-\rm dc}\propto\frac{P_0\gamma^e J_0^2(u)}{\overline{R_{\rm op}}+R_{\rm tot}}B_{y0}, \tag{11}$$

$$P_{x-\omega_m}\propto\frac{P_0\gamma^e J_0(u)J_1(u)}{\overline{R_{\rm op}}+R_{\rm tot}}\sin(\omega_m t)B_{x0}, \tag{12}$$

$$P_{x-2\omega_m}\propto\frac{P_0\gamma^e J_0(u)J_2(u)}{\overline{R_{\rm op}}+R_{\rm tot}}\cos(2\omega_m t)B_{y0}. \tag{13}$$

C. *X* mode: Modulation field on the transverse plane

As shown in Fig. 1(b), operating at the X mode with a modulation field $B_m\cos(\omega_m t)$ along the x axis, the field to be measured is defined as B_0. The presence of the modulation field makes the pump light insensitive to the slowly changing fields in the other two directions; thus, B_y and B_z are assumed to be zero. Components of $\mathbf{B}$ are $B_x=B_m\cos(\omega_m t)+B_0$, $B_y=0$, and $B_z=0$. Based on Eq. (1), the response of P_z for zero-order parametric modulation is observed to be

$$P_z(t)=\frac{(\overline{R_{\rm op}}+R_{\rm tot})\overline{R_{\rm op}}J_0(u)}{(\overline{R_{\rm op}}+R_{\rm tot})^2+(\gamma^e B_0)^2}\times\left\{J_0(u)+2\sum_{k=1}^{k=\infty}J_{2k}(u)\cos(2k\omega_m t)+\frac{2\gamma_e B_0}{\overline{R_{\rm op}}+R_{\rm tot}}\sum_{k=1}^{k=\infty}J_{2k-1}(u)\sin[(2k-1)\omega_m t]\right\}. \tag{14}$$

The term $(\gamma^e B_0)^2$ in the denominator can be ignored when $\overline{R_{\rm op}}+R_{\rm tot}\gg\gamma^e B_0$. In the zero field, its first harmonic of ω_m is approximately

$$P_{z-\omega_m}\propto\frac{\gamma^e\overline{R_{\rm op}}J_0(u)J_1(u)}{(\overline{R_{\rm op}}+R_{\rm tot})^2}\sin(\omega_m t)B_0. \tag{15}$$

However, for B_0 with a large variation range, the dc component of P_z can be obtained as

$$P_{z-\rm dc}\propto\frac{(\overline{R_{\rm op}}+R_{\rm tot})\overline{R_{\rm op}}J_0^2(u)}{(\overline{R_{\rm op}}+R_{\rm tot})^2+(\gamma^e B_0)^2}, \tag{16}$$

which appears as an absorption curve with B_0, the half-width at half maximum of which is consistent with the transverse relaxation rate $1/T_2=\overline{R_{\rm op}}+R_{\rm tot}$. Therefore, $1/T_2$ can be obtained according to the linewidth of the dc response in the X mode.

Equations (11)–(13) and (15) show that different harmonics are determined by their response coefficients, which contain Bessel series and the mutually restricted terms, $R_{\rm op}$ and $R_{\rm tot}$. Hence, the optimal sensitivity can be obtained by adjusting the amplitude and frequency of the modulation field with a proper pumping intensity. In addition, the responses of these two operation modes indicate that their detection directions are different, although they have similar solutions, as illustrated in Fig. 1.

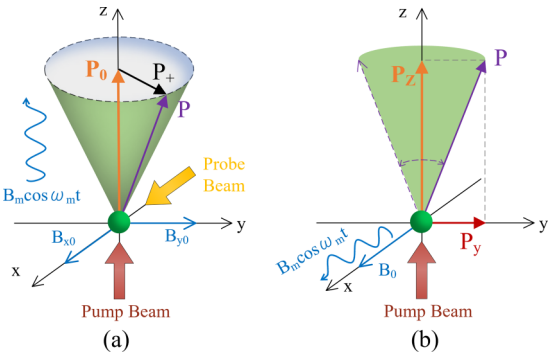

FIG. 1. Principle sketch of parametric modulation on an optically pumped atom. **P**, polarization of an alkali atom, where $P_+=P_x+iP_y$ and i is the imaginary number; $B_m\cos(\omega_m t)$, modulation field; and B_{x0}, B_{y0}, B_0, magnetic fields to be measured. (a) Z mode and (b) X-Mode.

III. EXPERIMENTAL SETUPS

A schematic of the experimental apparatus is shown in Fig. 2. A cubic vapor cell of 10-mm inner length contains a small droplet of K metal of natural abundance, 600 Torr of ^{4}He as a buffer gas, and 50 Torr of N_2 as a quenching gas. It is placed in a boron nitride ceramic oven, which is heated to 160 °C by twisted-pair wires using a 100-kHz ac current. A Pt1000 resistor pasted on the inner wall of

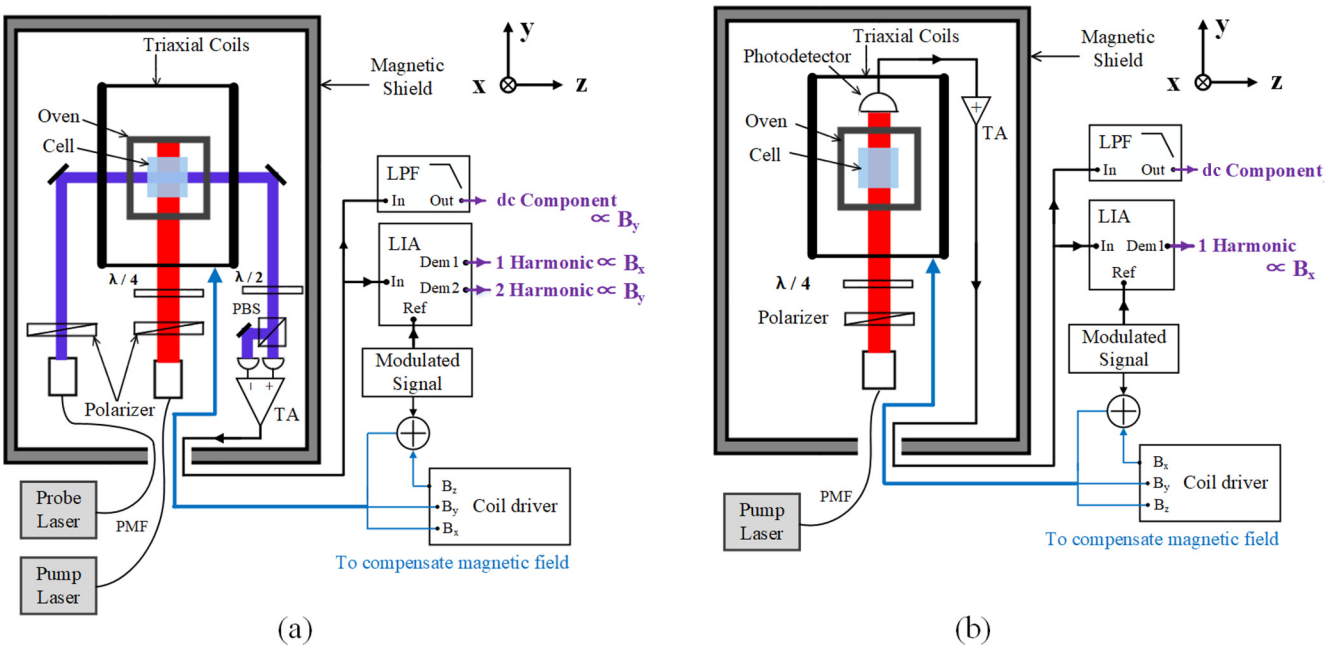

FIG. 2. Schematic of the experimental apparatus. PMF: polarization maintaining optical fiber. TA: transimpedance amplifier. PBS: polarization beam splitter. LIA: lock-in amplifier. LPF: low-pass filter. PD: photodiode. A circularly polarized pump beam propagating along the z axis is used to polarize the K vapor. (a) Modulation along the z axis with an additional linearly polarized probe beam propagating along the x axis and (b) modulation along the x axis.

the oven provides a real-time monitor of the cell temperature, so that the density of K is maintained at about $n_K = 2.24 \times 10^{13}$ cm^{-3} [28]. A four-layer cylindrical μ-metal shield is employed to isolate the external magnetic field interference.

The pump beam, tuned on the K D_1 resonance line at 770.110 nm, traverses along the z axis. A combination of a polarizer and a quarter-wave plate converts the linearly polarized pump beam into a circularly polarized one with a spot diameter of 3 mm. In the Z mode, an additional probe beam whose frequency (766.600 nm) is tuned to several gigahertz from the K D_2 resonance line is utilized to detect the polarization projection along the x axis. To suppress additional spin relaxation, the probe intensity is only 100 μW. Both light sources are New Focus external-cavity diode laser systems and illuminate into the vapor cell via a polarization-maintaining optical fiber.

A commercial computer-controlled digital lock-in amplifier (Zurich Instruments, model MFLI) is used as a demodulator to obtain the parametric response of each order. This is also the source that generates arbitrary modulation fields. The dc component is obtained by passing the output signal through a low-pass filter with a bandwidth of 100 Hz. The first or second harmonic is obtained to demodulate with a frequency of ω_m or $2\omega_m$. An analog adder (Stanford Research Systems, SIM980) applies the modulation field and compensation field to a triaxial coil system synchronously. A transimpedance amplifier (Thorlabs, PDA200C) amplifies the photocurrent induced by the photodiode.

In the Z mode, the polarization plane of a linearly polarized probe light will produce an optical rotation angle θ proportional to P_x when passing through the cell along the x axis. Considering the spatial distribution of P_x, this rotation angle θ can be expressed as [39]

$$\theta = \frac{1}{4} n_K r_e c f_{D2} \frac{\nu_{pr} - \nu_{D2}}{(\nu_{pr} - \nu_{D2})^2 + (\Gamma/2)^2} \int_L P_x dx, \tag{17}$$

where Γ is the pressure-broadened absorption linewidth, ν_{pr} is the frequency of the probe light, r_e is the classical electron radius, c is the speed of light, f_{D2} is the oscillator strength, ν_{D2} is the resonant frequency of the K D_2 line, and L is the length of the vapor cell.

θ is detected by the balanced polarimetry technique, as shown in Fig. 2(a) [28]. When $P_x \ll 1$, the signal response of the OPM can be approximated as

$$S_{Z\text{-mode}} = \eta I_{pr} \exp[-n_K \sigma_{op}(\nu_{pr}) L]\theta, \tag{18}$$

where η is a conversion factor between light and voltage, I_{pr} is the probe intensity.

In the X mode, the intensity variation of the circularly polarized pump light passing through the cell implies the information of P_z. Therefore, the OPM response can be directly obtained by monitoring the pump intensity behind the cell, which can be expressed as

$$S_{X-\text{mode}} = \eta I_{\text{pump}} \exp[-n_K \sigma_{op}(\nu_{\text{pump}}) L(1 - P_z)], \tag{19}$$

where I_{pump} and ν_{pump} are the initial intensity and the frequency of the pump light, respectively. When the change in P_z is small, the relationship between $S_{X-\text{mode}}$ and P_z can be considered to be approximately linear.

According to the experimental setups, the performance of the OPM operated in these two modes is investigated, and the experimental results are compared with our theoretical solutions.

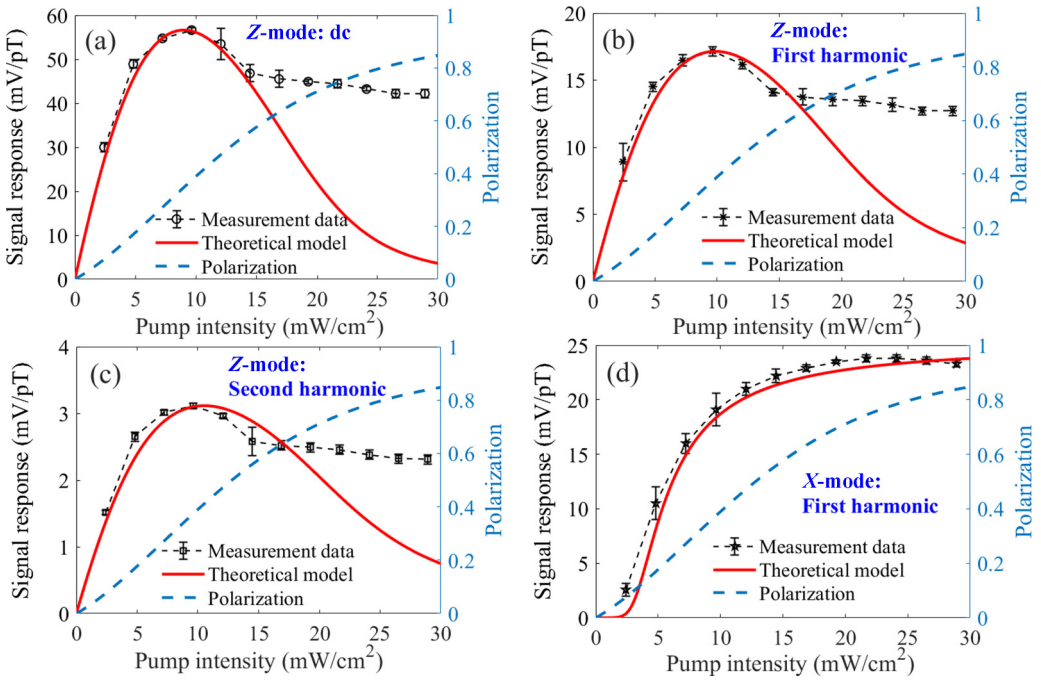

FIG. 3. Signal responses to weak magnetic fields and polarization of alkali atoms as a function of pump intensity. Modulation field: amplitude of 80 nT and frequency of 1 kHz. (a), (b), and (c) represent the response of the dc component, the first harmonic, and the second harmonic in the Z mode, respectively. Each response approaches the maximum at 10 mW/cm^2 by fitting with Eqs. (11)–(13). (d) represents the first-harmonic response, which increases with the pump intensity by fitting with Eqs. (14) and (19) in the X mode. The polarization of the alkali atoms increases with the pump-light intensity. Differences between actual responses and theoretical fitting curves are caused by the diffusion between atoms.

IV. RESULTS AND DISCUSSION

Parametric modulation would induce spin-exchange relaxation of atomic spins and alter the response strength. The ratio of B_m to ω_m determines the modulation index u of the Bessel series. Therefore, the value of B_m corresponding to the maximum response differs for different conditions. To explore the optimal sensitivity, several experiments were carried out.

First, the relationship between the pump intensity and the response was studied with a modulation field of 80 nT at 1 kHz, as depicted in Fig. 3. For different axes, the calibration signal was an identical sinusoidal field of 100 pT at 20 Hz. The normalized response strengths at different pump intensities are plotted on the left axis. The experimental data in Figs. 3(a) and 3(c) were fitted with the coefficients of B_{y0} in Eqs. (11) and (13), respectively. Figure 3(b) was fitted with the coefficient of B_{x0} in Eq. (12). The response strength reached the maximum when the pump intensity was 10 mW/cm^2 in the Z mode. In the X mode, the experimental data in Fig. 3(d) were fitted with the coefficient of B_0 according to Eq. (19), indicating that the response strength increased with the pump intensity since its scale factor of B_0 contained I_{pump}. The polarization of alkali-metal atoms is plotted against on right axis in Fig. 3, based on the theoretical values of $\overline{R_{\text{op}}}$ and R_{rel}. Differences between theoretical fitting curves and actual measurements are the result of the diffusion phenomenon [40].

Then, the response strength was measured with the amplitude of the modulation field applied under different modulation frequencies. In the Z mode, the experimental data in Figs. 4(a) and 4(c) were fitted with the coefficient of B_{y0} in Eqs. (11) and (13), respectively. The experimental data in Fig. 4(b) were fitted with the coefficient of B_{x0} in Eq. (12).

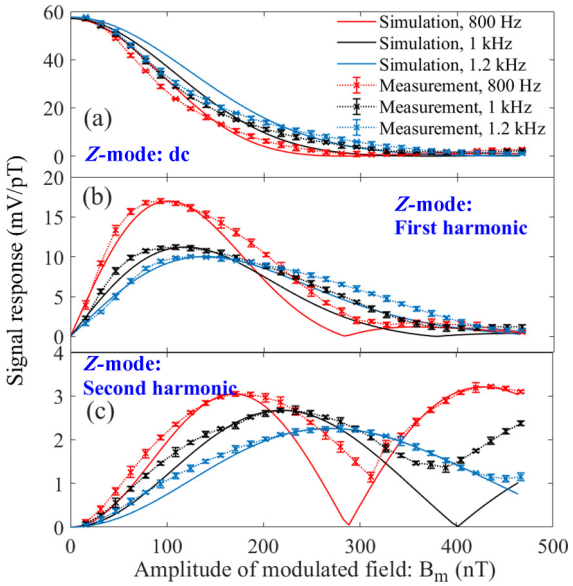

FIG. 4. Measurement and simulation in the Z mode, with modulation frequencies of 800 Hz, 1 kHz, and 1.2 kHz; the pump intensity is 10 mW/cm^2. The response strength is a function of the modulation index.

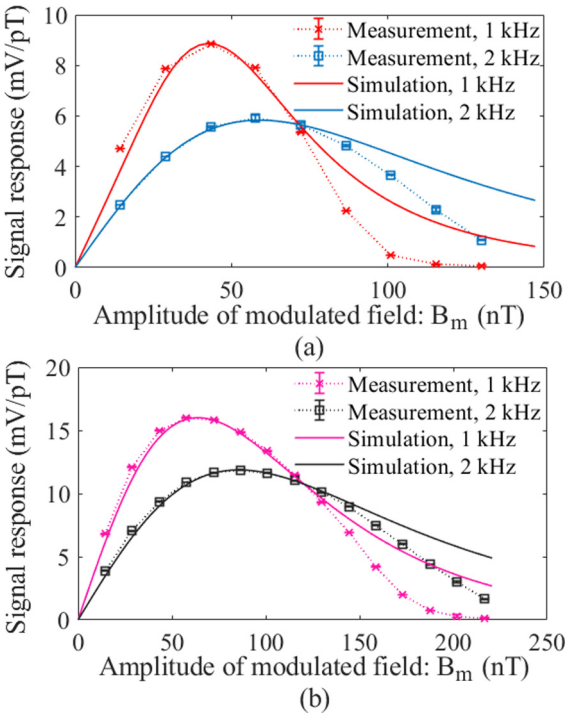

FIG. 5. Measurement and simulation in the X mode with modulation frequencies of 1 and 2 kHz. (a) Pump density of 2.5 $\mathrm{mW/cm^2}$ and (b) pump density of 5 $\mathrm{mW/cm^2}$. The response strength is a function of the pump-light intensity and the modulation index.

In the X mode, the experimental data in Fig. 5(d) were fitted with the coefficient of B_0 in Eq. (15). This verifies that the response strength is a function of the modulation index. Because the higher-order Bessel series terms are neglected and the nonuniformity of the polarization distribution affects the pumping rate and the slowing-down factor, the actual measurement results are slightly different from the theoretical values but are still within acceptable range.

Figure 6 shows the normalized responses at different modulation frequencies. The amplitude B_m is 80 nT. The pump density is 5 $\mathrm{mW/cm^2}$. The error bars of the experimental data are smaller than the data markers, so they are not plotted. This implies that with a higher modulation frequency, it is necessary to increase the value of B_m, which yields a stronger spin-exchange effect and reduces the response strength.

In the X mode, the transverse relaxation rate was measured using the linewidth of the dc response, as shown in Fig. 7. The pumping rate was calculated with the proposed average model. The experimental data are consistent with the theoretical values, indicating that the proposed average pumping model is effective.

Based on the above analysis and experiments, it can be concluded that the optimal response strength can be obtained by controlling the pump-light intensity and the modulation index to quickly identify the best sensitivity of the magnetometer system.

The optimal responses of the first and second harmonics in the Z mode were obtained with modulation fields of 90 nT at 800 Hz and 170 nT at 800 Hz with a pump intensity of 10 $\mathrm{mW/cm^2}$, respectively. Figure 8(a) exhibits the noise

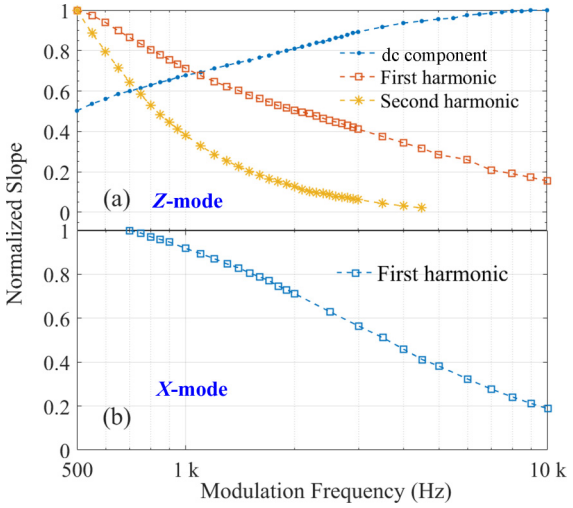

FIG. 6. Normalized response of a modulation field with an amplitude of $B_m = 80$ nT. With a fixed B_m, the response strength decreased with increasing modulation frequency.

spectral density of each harmonic working at the optimal response in the Z mode, while that of the X mode operating at optimal response under different pump intensities is shown in Fig. 8(b). The $1/f$ noises are not obvious, and low-frequency noises are suppressed.

In a dual-beam structure, the Z mode, the pump light is parallel to the modulation field; therefore, the modulation field does not affect the polarization along the z axis. The precession of the atomic magnetic moment reaches the dynamic equilibrium under the combined action of the pump light and the modulation field. The polarizing detection method of the balanced polarization suppresses the common-mode noise in the detection system. Therefore, a sensitivity of nearly 10 $\mathrm{fT/Hz^{1/2}}$ can be obtained with the first harmonic in the Z mode.

Nevertheless, in a single-beam structure, the X mode, the first harmonic of the pump-light intensity behind the vapor cell reflects the magnetic field to be measured. For a pump light with a weak initial intensity, a large modulation field

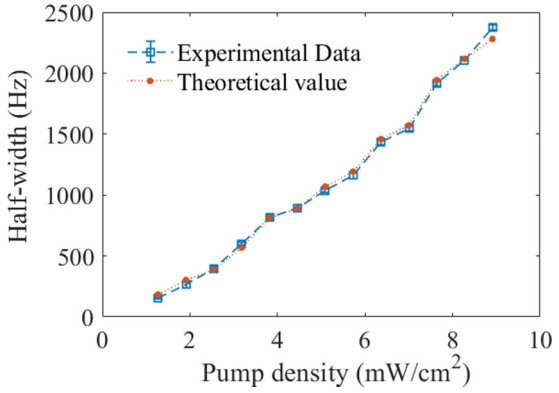

FIG. 7. Linewidth of the dc response in the X mode as a function of the pump intensity, related to $\overline{R_{\mathrm{op}}}$. The half-width represents the transverse relaxation rate $1/T_2$. The experimental data match the theoretical value.

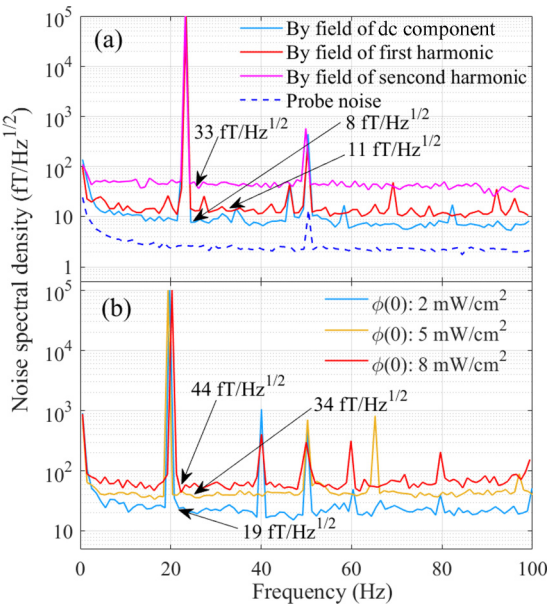

FIG. 8. Noise spectral density of the two operation modes. (a) Z mode: a modulation field at 90 nT at 800 Hz when measuring the dc component and first harmonic and 170 nT at 800 kHz when measuring the second harmonic. The calibration field is 100 pT at 23 Hz. The probe noise is 2.5 $\mathrm{fT/Hz^{1/2}}$, far less than the total noise. (b) X mode: with different pump densities of 2, 5, and 8 $\mathrm{mW/cm^2}$, the optimal modulation field is 35, 70, and 100 nT at 1 kHz, respectively. The calibration field is 100 pT at 20 Hz. The noise baseline is limited by the magnetic-field noise and the system noise.

leads to a great spin-exchange relaxation. It causes strong absorption of the pump light by atoms and eventually decreases the output light intensity. Moreover, increasing the pump-light intensity will increase its dc response, resulting in a larger photocurrent bias in the photodiode (PD). Through a preamplifier, the first harmonic is amplified with the offset of the photocurrent, which leads to a limited magnification. At the same time, excessive light intensity will deteriorate the signal-to-noise ratio performance, which is mainly induced by the increased shot noise on the PD. Therefore, the key factor for the improvement of the sensitivity is the employment of a weak pump-light intensity and the application of a low-frequency modulation field with optimal amplitude.

V. CONCLUSION

In summary, we have theoretically and experimentally examined the effect of pump-light intensity and the modulation field of OPMs under zero-field parametric modulation. The analytic solutions of different harmonic responses were investigated with the average-pumping-rate model. In the Z mode, the balanced polarimetry technique can suppress the common-mode noise and offer natural advantages of high sensitivity. However, the X mode requires fewer optical components and has the advantage of small volume integration due to its configuration of a single laser beam. Compared with the nonmodulated SERF magnetometers, the atomic spins after modulation exhibit strong spin-exchange relaxation. Therefore, the parameter selection of the modulation field and the pump-light intensity become the key factors in the improvement of OPM performance. Since the response is modulated into several kilohertz, it is beneficial to suppress the $1/f$ noise, especially the low-frequency noise caused by vibrations and detection systems. Parametric modulation is especially suitable for magnetocardiography and magnetoencephalography. The presented theory and method in this paper have profound guiding significance for the application of parametric modulation technique in OPMs.

ACKNOWLEDGMENTS

This work was supported by the National Key R&D Program of China (Grant No. 2018YFB2002405) and National Natural Science Foundation of China (Grant No. 61627806).

[1] D. Budker and D. F. J. Kimball, *Optical Magnetometry* (Cambridge University Press, Cambridge, 2013).
[2] H. G. Dehmelt, Modulation of a light beam by precessing absorbing atoms, Phys. Rev. **105**, 1924 (1957).
[3] W. E. Bell and A. L. Bloom, Optical detection of magnetic resonance in alkali metal vapor, Phys. Rev. **107**, 1559 (1957).
[4] A. L. Bloom, Principles of operation of the rubidium vapor magnetometer, Appl. Opt. **1**, 61 (1962).
[5] V. Schultze, R. Ijsselsteijn, T. Scholtes, S. Woetzel, and H.-G. Meyer, Characteristics and performance of an intensity-modulated optically pumped magnetometer in comparison to the classical Mx magnetometer, Opt. Express **20**, 14201 (2012).
[6] E. B. Alexandrov, M. V. Balabas, A. K. Vershovski, and A. Pazgalev, Experimental demonstration of the sensitivity of an optically pumped quantum magnetometer, Tech. Phys. **49**, 779 (2004).
[7] S. P. Krzyzewski, A. R. Perry, V. Gerginov, and S. Knappe, Characterization of noise sources in a microfabricated single-beam zero-field optically-pumped magnetometer, J. Appl. Phys. **126**, 044504 (2019).
[8] P. D. D. Schwindt, B. Lindseth, S. Knappe, V. Shah, and J. Kitching, Chip-scale atomic magnetometer with improved sensitivity by use of the M_x technique, Appl. Phys. Lett. **90**, 081102 (2007).
[9] S. Volkmar, S. Bastian, I. Rob, T. Scholtes, and S. Woetzel, An optically pumped magnetometer working in the light-shift dispersed Mz mode, Sensors **17**, 561 (2017).
[10] E. B. Alexandrov, Recent progress in optically pumped magnetometers, Phys. Scr. **T105**, 27 (2003).
[11] J. C. Allred, R. N. Lyman, T. W. Kornack, and M. V. Romalis, High-Sensitivity Atomic Magnetometer Unaffected by Spin-Exchange Relaxation, Phys. Rev. Lett. **89**, 130801 (2002).
[12] I. K. Kominis, T. W. Kornack, J. C. Allred, and M. V. Romalis, A subfemtotesla multichannel atomic magnetometer, Nature (London) **422**, 596 (2003).
[13] R. E. Slocum and B. I. Marton, Measurement of weak magnetic fields using zero-field parametric resonance in optically pumped He_4, IEEE Trans. Magn. **9**, 221 (1973).
[14] C. Cohen-Tannoudji, J. Dupont-Roc, S. Haroche, and F. Laloë, Diverse résonances de croisement de niveaux sur des atomes

pompés optiquement en champ nul. I. théorie, Rev. Phys. Appl. **5**, 95 (1970).

[15] I. Savukov, Y. J. Kim, V. Shah, and M. G. Boshier, Highsensitivity operation of single-beam optically pumped magnetometer in a kHz frequency range, Meas. Sci. Technol. **28**, 035104 (2017).

[16] R. Zhang, Z. Wang, X. Peng, W. Li, S. Li, and H. Guo, Spin dynamics of magnetic resonance with parametric modulation in a potassium vapor cell, Chin. Phys. B **26**, 030701 (2017).

[17] J. Li, P. Du, J. Fu, X. Wang, Q. Zhou, and R. Wang, Miniature quad-channel spin-exchange relaxation-free magnetometer for magnetoencephalography, Chin. Phys. B **28**, 040703 (2019).

[18] E. Boto, N. Holmes, J. Leggett, G. Roberts, V. Shah, S. S. Meyer, L. D. Muñoz, K. J. Mullinger, T. M. Tierney, S. Bestmann, G. R. Barnes, R. Bowtell, and M. J. Brookes, Moving magnetoencephalography towards realworld applications with a wearable system, Nature (London) **555**, 657 (2018).

[19] G. Roberts, N. Holmes, N. Alexander, E. Boto, J. Leggett, R. M. Hill, V. Shah, M. Rea, R. Vaughan, E. A. Maguire, K. Kessler, S. Beebe, M. Fromhold, G. R. Barnes, R. Bowtell, and M. J. Brookes, Towards OPMMEG in a virtual reality environment, NeuroImage **199**, 408 (2019).

[20] R. M. Hill, E. Boto, N. Holmes, C. Hartley, Z. A. Seedat, J. Leggett, G. Roberts, V. Shah, T. M. Tierney, M. W. Woolrich, C. J. Stagg, G. R. Barnes, R. R. Bowtell, R. Slater, and M. J. Brookes, A tool for functional brain imaging with lifespan compliance, Nat. Commun. **10**, 4785 (2019).

[21] V. Shah and M. V. Romalis, Spin-exchange relaxationfree magnetometry using elliptically polarized light, Phys. Rev. A **80**, 013416 (2009).

[22] J. Osborne, J. Orton, O. Alem, and V. Shah, Fully integrated, standalone zero field optically pumped magnetometer for biomagnetism, in *Steep Dispersion Engineering and Opto-Atomic Precision Metrology XI*, edited by S. M. Shahriar and J. Scheuer (SPIE, 2018), Vol. 10548.

[23] R. Mhaskar, S. Knappe, and J. Kitching, A low-power, high-sensitivity micromachined optical magnetometer, Appl. Phys. Lett. **101**, 241105 (2012).

[24] V. K. Shah and R. T. Wakai, A compact, high performance atomic magnetometer for biomedical applications, Phys. Med. Biol. **58**, 8153 (2013).

[25] D. Sheng, A. R. Perry, S. P. Krzyzewski, S. Geller, J. Kitching, and S. Knappe, A microfabricated optically-pumped magnetic gradiometer, Appl. Phys. Lett. **110**, 031106 (2017).

[26] Z. Li, R. T. Wakai, and T. G. Walker, Parametric modulation of an atomic magnetometer, Appl. Phys. Lett. **89**, 134105 (2006).

[27] G. Zhang, S. Huang, F. Xu, Z. Hu, and Q. Lin, Multichannel spin exchange relaxation free magnetometer towards two-dimensional vector magnetoencephalography, Opt. Express **27**, 597 (2019).

[28] S. J. Seltzer, Developments in alkali-metal atomic magnetometry, Ph.D. dissertation, Dept. physics, Princeton University, 2008.

[29] L. Chen, B. Zhou, G. Lei, W. Wu, Y. Zhai, Z. Wang, and J. Fang, Effects of temperature on Rb and 129^{Xe} spin polarization in a nuclear magnetic resonance gyroscope with low pump power, AIP Adv. **7**, 115101 (2017).

[30] Y. Jia, Z. Liu, B. Zhou, X. Liang, W. Wu, J. Peng, M. Ding, Y. Zhai, and J. Fang, Pump beam influence on spin polarization homogeneity in the nuclear magnetic resonance gyroscope, J. Phys. D **52**, 355001 (2019).

[31] L. Jiang, W. Quan, Y. Liang, J. Liu, L. Duan, and J. Fang, Effects of pump laser power density on the hybrid optically pumped comagnetometer for rotation sensing, Opt. Express **27**, 27420 (2019).

[32] J. Lu, Z. Qian, J. Fang, and W. Quan, Effects of AC magnetic field on spin-exchange relaxation of atomic magnetometer, Appl. Phys. B **122**, 59 (2016).

[33] J. Zhao, M. Ding, J. Lu, K. Yang, D. Ma, H. Yao, B. Han, and G. Liu, Determination of spin polarization in spin-exchange relaxation-free atomic magnetometer using transient response, IEEE Trans. Instrum. Meas., **69**, 845 (2020).

[34] J. Lu, Z. Qian, and J. Fang, A fast determination method for transverse relaxation of spin-exchange-relaxation-free magnetometer, Rev. Sci. Instrum. **86**, 043104 (2015).

[35] S. Kadlecek, L. W. Anderon, and T. Walker, Measurement of potassium-potassium spin relaxation cross sections, Nucl. Instrum. Meth. Phys. Res., Sect. A **402**, 208 (1998).

[36] F. A. Franz and C. Volk, Electronic spin relaxation of the $4^2S_{1/2}$ state of K induced by K-He and K-Ne collisionfs, Phys. Rev. A **26**, 85 (1982).

[37] R. H. S. N. W. Ressler and T. E. Stark, Measurement of spin-exchange cross sections for Cs^{133}, Rb^{87}, K^{39}, and Na^{23}, Phys. Rev. **184**, 102 (1969).

[38] M. P. Ledbetter, I. M. Savukov, V. M. Acosta, D. Budker, and M. V. Romalis, Spin-exchange-relaxation-free magnetometry with Cs vapor, Phys. Rev. A **77**, 033408 (2008).

[39] Y. Ito, D. Sato, K. E. Kamada, and T. Kobayashi, Optimal densities of alkali metal atoms in an optically pumped KRb hybrid atomic magnetometer considering the spatial distribution of spin polarization, Opt. Express **24**, 15391 (2016).

[40] M. Natsuhiko, O. Kazuhisa, B. Kazuhiro, I. Sunao, T. Akira, and K. Tetsuo, A plateau in the sensitivity of a compact optically pumped atomic magnetometer, AIP Adv. **4**, 057132 (2014).